INSTITUTE OF PHYSICS PUBLISHING NANOTECHNOLOGY
Nanotechnology **17** (2006) S34–S47 doi:10.1088/0957-4484/17/4/007

Towards ferrofluidics for μ-TAS and lab on-a-chip applications

Leidong Mao and Hur Koser

Department of Electrical Engineering, Yale University, 15 Prospect Street, New Haven, CT 06520, USA

E-mail: hur.koser@yale.edu

Received 18 July 2005, in final form 3 November 2005
Published 25 January 2006
Online at stacks.iop.org/Nano/17/S34

Abstract
In this paper, we show that ferrofluids can be pumped very effectively in closed-channel geometries both in the macro- and micro-scales using spatially travelling, sinusoidally time-varying magnetic fields. The results from numerical modelling demonstrate that the optimum pumping frequency is the reciprocal of the Brownian relaxation time constant of the magnetic nanoparticles inside the ferrofluid. Since the Brownian time constant depends in part on the overall hydrodynamic volume of the magnetic nanoparticles, this work has been carried with a view to developing functionalized ferrofluids that can be used as sensitive pathogen detectors in the context of ferrohydrodynamic pumping via travelling magnetic fields. A micro-ferrofluidic device has been designed and fabricated in order to demonstrate the potential development of this technology for pathogen detection. A cost-effective fabrication process combining insulated metal substrate etching and soft lithography is used to realize the prototype micro-ferrofluidic device. Results show good agreement between simulation and experiment. We finally propose a ferrofluid-based pathogen detection scheme that is expected to be insensitive to temperature and viscosity differences between the ferrofluid and the sample to be tested.

(Some figures in this article are in colour only in the electronic version)

1. Introduction

Ferrofluids are stable colloidal suspensions of nanosize magnetic particles in a liquid, which may be either an aqueous or a non-polar solvent. The nanoparticles are coated with a stabilizing dispersing agent (surfactant), which is matched to the liquid type and will prevent agglomeration by overcoming the attractive van der Waals forces between the particles [1]. A magnetic field gradient, combined with liquid viscous forces, allows continuous actuation and precise positioning of a ferrofluid segment in a flow channel. Ferrofluids have found their way into a variety of applications, such as sealing, damping and blood separation [2]. In dilute, functionalized forms, ferrofluids have also been used as drug delivery and MRI contrast agents [3, 4]. Ferrofluids offer attractive alternatives to moving mechanical components in miniaturized cooling, pumping and integrated micro-total-analysis-systems (μ-TAS) for chip-scale chemistry and biology [5–8]. Water-based ferrofluids can be made bio-compatible, rendering them useful in novel cell manipulation and sorting schemes [3, 4].

Actuation of ferrofluids using only external magnetic fields offers the possibility of compact, reliable and simple fluid manipulation schemes both on macro- and micro-scales. However, most of these schemes have so far focused on magnetic forces acting on the free ferrofluid surface and on utilizing these forces to pump a secondary, non-magnetic fluid. As a result, the application potential of these schemes as compact and integrated pumps is limited by practical considerations, such as the compatibility and mixing potential of the two fluids and the surface properties of the channel walls, or the need for external moving permanent magnets [5, 6]. What is needed is an approach that allows pumping ferrofluids themselves in closed-loop geometries at multiple scales, enabling various applications ranging from integrated cooling systems to implantable drug delivery and cellular manipulation devices. In this fashion, ferrofluid chemistry and composition

can be engineered for the specific application at hand, and the same actuation scheme can be employed for virtually all types of ferrofluids.

This paper presents a study of a novel ferrofluid actuation scheme based on spatially travelling sinusoidal magnetic fields. Section 2 introduces ferrohydrodynamics and the modelling approach used to study the effects of geometry and excitation dynamics on ferrofluid pumping inside a closed-loop channel. It is shown that, under travelling magnetic field excitation, maximum pumping is achieved when the excitation frequency is comparable to the reciprocal of the Brownian relaxation time constant of the magnetic nanoparticles. This relaxation time is determined by the nanoparticles' effective hydrodynamic diameter, which depends in part on the type and size of the chemicals coating their surface. Section 3 discusses the initial results from a macro-scale ferrofluid pumping rig used to study ferrohydrodynamics, and section 4 presents the simulation, design, fabrication and initial testing of a micro-scale, integrated ferrofluidic pump.

The dependence of the maximum pumping frequency on the Brownian relaxation time constant of the magnetic nanoparticles is significant in the context of pathogen detection. Introducing minute quantities of a given molecule that binds to the surface of the magnetic nanoparticles will significantly shift the frequency of the ferrohydrodynamic pumping peak, suggesting a very effective and simple mechanism to use the MEMS ferrofluidic devices as highly sensitive, miniaturized, integrated and disposable pathogen detectors. In this context, the discussion concludes by focusing on the potential advantages of integrated pathogen detectors based on ferrohydrodynamic pumping over other micro-scale pathogen detection schemes (section 5).

2. Theory

Ferrohydrodynamic pumping in spatially uniform, sinusoidally time-varying magnetic fields has been studied extensively in the past [9]. Here we examine a different case where the applied sinusoidal field is a spatially travelling wave [10]. Actuation using travelling waves involves magnetic body forces and torque on the magnetic moment of the nanoparticles, both of which affect the overall pumping. In this study, ferrofluid body actuation under the influence of a travelling wave magnetic field is investigated in the most general case. A second order central-differencing scheme is employed iteratively to calculate the magnetic field strength inside the ferrofluid, as well as the flow and spin velocities of the magnetic particles. The ferrofluid is assumed to be monodisperse and magnetically linear.

2.1. Governing dynamics

2.1.1. Magnetization constitutive law. The magnetization relaxation equation for a ferrofluid undergoing simultaneous magnetization, convection with position dependent velocity $\mathbf{v}$, and reorientation due to particle spin $\boldsymbol{\omega}$ is [1]

$$\frac{\partial \mathbf{M}}{\partial t} + (\mathbf{v}\cdot\nabla)\,\mathbf{M} - \boldsymbol{\omega}\times\mathbf{M} + \frac{1}{\tau}\left[\mathbf{M} - \chi_0\mathbf{H}\right] = 0 \qquad (1)$$

where τ is a relaxation time constant and χ_0 is the effective magnetic susceptibility. In this work, the magnetic susceptibility is taken to be a constant. $\mathbf{M}$ is the magnetization and $\mathbf{H}$ is the magnetic field vector. In our modelling, we consider a cylindrical ferrofluid section as shown in figure 1. By symmetry, the flow velocity has only a z-directed component and the particle angular velocity has only a θ-directed component. Both velocities will change with the r coordinate, i.e.

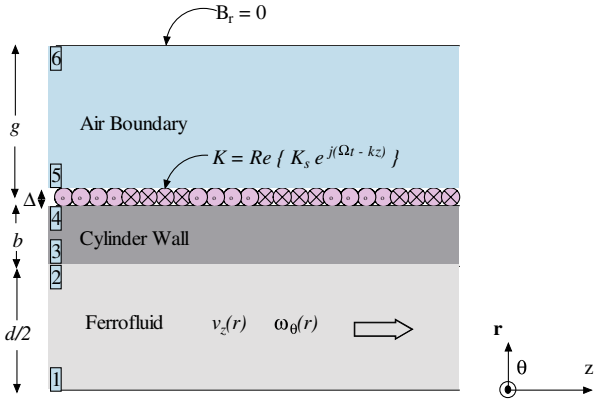

Figure 1. The set-up of the multilayered boundary problem. A ferrofluid segment inside a cylinder is magnetically stressed by a spatially travelling sinusoidal current sheet (only half of the cylinder is shown because of the symmetry). The air layer is taken thick enough to represent an infinite boundary, whereas Δ is infinitesimally small.

$$\mathbf{v} = v_z(r)\mathbf{i}_\mathbf{z}, \qquad \boldsymbol{\omega} = \omega_\theta(r)\mathbf{i}_\theta. \qquad (2)$$

2.1.2. Fluid mechanics. For incompressible fluids

$$\nabla\cdot\mathbf{v} = 0 \qquad \nabla\cdot\boldsymbol{\omega} = 0 \qquad (3)$$

where $\mathbf{v}$ is the linear fluid velocity and $\boldsymbol{\omega}$ is particle angular velocity. The coupled linear and angular momentum conservation equations for force density $\mathbf{f}$ and torque density $\mathbf{T}$ for a ferrofluid are [1]

$$\rho\left[\frac{\partial \mathbf{v}}{\partial t} + (\mathbf{v}\cdot\nabla)\,\mathbf{v}\right] = -\nabla p + \mathbf{f} + 2\zeta\nabla\times\boldsymbol{\omega} + (\zeta+\eta)\,\nabla^2\mathbf{v} \quad (4)$$

$$I\left[\frac{\partial \boldsymbol{\omega}}{\partial t} + (\mathbf{v}\cdot\nabla)\,\boldsymbol{\omega}\right] = \mathbf{T} + 2\zeta\,(\nabla\times\mathbf{v} - 2\boldsymbol{\omega}) + \eta'\nabla^2\boldsymbol{\omega} \quad (5)$$

where ρ is the mass density, p is the pressure, ξ is the vortex viscosity, η is the dynamic viscosity, I is the moment of inertia density, and η' is the shear coefficient of spin viscosity. At steady state, without inertial effects, equations (4) and (5) in cylindrical coordinates become

$$(\zeta+\eta)\left(\frac{\mathrm{d}^2 v_z}{\mathrm{d}r^2} + \frac{1}{r}\frac{\mathrm{d}v_z}{\mathrm{d}r}\right) + 2\zeta\left(\frac{\mathrm{d}\omega_\theta}{\mathrm{d}r} + \frac{\omega_\theta}{r}\right) - \frac{\mathrm{d}p'}{\mathrm{d}z} + \langle f_z\rangle = 0 \qquad (6)$$

$$\eta'\left(\frac{\mathrm{d}^2\omega_\theta}{\mathrm{d}r^2} + \frac{1}{r}\frac{\mathrm{d}\omega_\theta}{\mathrm{d}r} - \frac{\omega_\theta}{r^2}\right) - 2\zeta\left(\frac{\mathrm{d}v_z}{\mathrm{d}r} + 2\omega_\theta\right) + \langle T_\theta\rangle = 0. \qquad (7)$$

2.2. Magnetic field calculation

The travelling wave current sheet in figure 1 introduces a travelling wave magnetic field inside the cylindrical channel. Because of symmetry, there is no θ component of the magnetic field. Therefore, the total magnetic field $\mathbf{H}$, the magnetization $\mathbf{M}$ and the magnetic flux density $\mathbf{B}$ inside the ferrofluid are given by

$$\begin{aligned}\mathbf{H} &= \mathrm{Re}\left\{\left(\widehat{H}_r(r)\mathbf{i}_r + \widehat{H}_z(r)\mathbf{i}_\mathbf{z}\right)\cdot \mathrm{e}^{\mathrm{j}(\Omega t - kz)}\right\}\\ \mathbf{M} &= \mathrm{Re}\left\{\left(\widehat{M}_r(r)\mathbf{i}_r + \widehat{M}_z(r)\mathbf{i}_\mathbf{z}\right)\cdot \mathrm{e}^{\mathrm{j}(\Omega t - kz)}\right\}\\ \mathbf{B} &= \mathrm{Re}\left\{\left(\widehat{B}_r(r)\mathbf{i}_r + \widehat{B}_z(r)\mathbf{i}_\mathbf{z}\right)\cdot \mathrm{e}^{\mathrm{j}(\Omega t - kz)}\right\}\end{aligned} \tag{8}$$

where Ω is the frequency of the travelling wave, and k is its wavenumber.

We would like to solve for magnetization in terms of the field amplitudes. Substituting (8) into (1) relates the magnetization components to the magnetic field $\mathbf{H}$

$$\begin{aligned}\widehat{M}_r &= \chi_0\frac{\left\{\left[\mathrm{j}\left(\Omega\tau - kv_z\tau\right)+1\right]\widehat{H}_r + \omega_\theta\tau\widehat{H}_z\right\}}{\left[\mathrm{j}\left(\Omega\tau - kv_z\tau\right)+1\right]^2 + (\omega_\theta\tau)^2}\\ &= C(r)\widehat{H}_r + D(r)\widehat{H}_z\\ \widehat{M}_z &= \chi_0\frac{\left\{-\omega_\theta\tau\widehat{H}_r + \left[\mathrm{j}\left(\Omega\tau - kv_z\tau\right)+1\right]\widehat{H}_z\right\}}{\left[\mathrm{j}\left(\Omega\tau - kv_z\tau\right)+1\right]^2 + (\omega_\theta\tau)^2}\\ &= -D(r)\widehat{H}_r + C(r)\widehat{H}_z\end{aligned}. \tag{9}$$

where

$$\begin{aligned}C(r) &= \chi_0\frac{\mathrm{j}\left(\Omega\tau - kv_z\tau\right)+1}{\left[\mathrm{j}\left(\Omega\tau - kv_z\tau\right)+1\right]^2 + (\omega_\theta\tau)^2}\\ D(r) &= \chi_0\frac{\omega_\theta\tau}{\left[j\left(\Omega\tau - kv_z\tau\right)+1\right]^2 + (\omega_\theta\tau)^2}.\end{aligned} \tag{10}$$

In general, $C(r)$ and $D(r)$ are r-position dependent through the position dependence of $\mathbf{v}$ and $\boldsymbol{\omega}$. Within the current-free ferrofluid, Gauss's law for the magnetic flux density and Ampere's law for the magnetic field require the imposed fields to satisfy

$$\begin{aligned}\nabla\times\mathbf{H} = \mathbf{0} &\Rightarrow \widehat{H}_r(r) = \frac{\mathrm{j}}{k}\frac{\mathrm{d}\widehat{H}_z(r)}{\mathrm{d}r}\\ \nabla\cdot\mathbf{B} = \mathbf{0} &\Rightarrow \frac{\mathrm{d}\widehat{B}_r}{\mathrm{d}r} + \frac{\widehat{B}_r}{r} - \mathrm{j}k\widehat{B}_z = 0\end{aligned} \tag{11}$$

where

$$\mathbf{B} = \mu_0\left(\mathbf{H}+\mathbf{M}\right). \tag{12}$$

Substituting (12) into (11), together with (8)–(10), yields the magnetic field equation

$$\begin{aligned}&\frac{\mathrm{d}^2\widehat{H}_z(r)}{\mathrm{d}r^2} + \left[\frac{1}{1+C(r)}\frac{\mathrm{d}C(r)}{\mathrm{d}r} + \frac{1}{r}\right]\frac{\mathrm{d}\widehat{H}_z(r)}{\mathrm{d}r}\\ &\quad + \left[\frac{-\mathrm{j}k}{1+C(r)}\left(\frac{D(r)}{r} + \frac{\mathrm{d}D(r)}{\mathrm{d}r}\right) - k^2\right]\widehat{H}_z(r) = 0.\end{aligned} \tag{13}$$

2.3. Magnetic boundary conditions

In order to solve equation (13) to determine the magnetic field throughout the ferrofluid, one needs to specify the boundary conditions for the magnetic field equation, which can be done by employing the general magnetic diffusion equation [11]

$$\frac{1}{\mu\sigma}\nabla^2\mathbf{B} = \left(\frac{\partial\mathbf{B}}{\partial t} + (\mathbf{v}\cdot\nabla)\right)\mathbf{B}. \tag{14}$$

Note that (14) is only valid for material layers outside the ferrofluid.

In general, for the isotropic material layers shown in figure 1, one gets the following diffusion transfer relations:

$$\begin{aligned}\begin{pmatrix}\widehat{B}_{4,r}\\ \widehat{B}_{3,r}\end{pmatrix} &= -\frac{\mathrm{j}\mu}{k}\begin{pmatrix}f_0(d/2, d/2+b) & g_0(d/2+b, d/2)\\ g_0(d/2, d/2+b) & f_0(d/2+b, d/2)\end{pmatrix}\\ &\quad\times\begin{pmatrix}\widehat{H}_{4,z}\\ \widehat{H}_{3,z}\end{pmatrix}\\ \begin{pmatrix}\widehat{B}_{6,r}\\ \widehat{B}_{5,r}\end{pmatrix} &= -\frac{\mathrm{j}\mu}{k}\begin{pmatrix}f_0(d/2+b+\Delta, d/2+b+g) & g_0(d/2+b+g, d/2+b+\Delta)\\ g_0(d/2+b+\Delta, d/2+b+g) & f_0(d/2+b+g, d/2+b+\Delta)\end{pmatrix}\begin{pmatrix}\widehat{H}_{6,z}\\ \widehat{H}_{5,z}\end{pmatrix}\\ f_0\left(r_\alpha, r_\beta\right) &= \frac{k\left[K_0\left(kr_\alpha\right)I_0'\left(kr_\beta\right) - I_0\left(kr_\alpha\right)K_0'\left(kr_\beta\right)\right]}{I_0\left(kr_\alpha\right)K_0\left(kr_\beta\right) - I_0\left(kr_\beta\right)K_0\left(kr_\alpha\right)}\\ g_0\left(r_\alpha, r_\beta\right) &= \frac{1}{\left[I_0\left(kr_\alpha\right)K_0\left(kr_\beta\right) - I_0\left(kr_\beta\right)K_0\left(kr_\alpha\right)\right]r_\alpha}.\end{aligned} \tag{15}$$

Here μ is the material's magnetic permeability, k is the wavenumber, and $\widehat{H}_z$ is the complex amplitude of the z-directed magnetic field at the surface indicated by the numeric subscript. I_0 and K_0 are the modified Bessel functions. The field boundary conditions at the material interface are

$$B_{5,r} = B_{4,r}, \qquad B_{6,r} = B_{6,z} = 0, \qquad H_{4,z} - H_{5,z} = K_\mathrm{s}. \tag{16}$$

Once (15) and (16) are solved, one can find the complex field amplitude at each boundary surface as a function of the amplitude, K_s, of the travelling wave current sheet at the outer tube wall.

2.4. Magnetic force and torque densities

For $0 \leqslant r \leqslant d/2$, i.e., inside the ferrofluid, the magnetic force density is [1]

$$\mathbf{f} = \mu_0\left(\mathbf{M}\cdot\nabla\right)\mathbf{H}. \tag{17}$$

The time average components of the force density are then given by

$$\begin{aligned}\langle f_r\rangle &= \frac{1}{2}\mu_0\mathrm{Re}\left[\widehat{M}_r\frac{\mathrm{d}\widehat{H}_r^*}{\mathrm{d}r} + \mathrm{j}k\widehat{M}_z\widehat{H}_r^*\right]\\ \langle f_z\rangle &= \frac{1}{2}\mu_0\mathrm{Re}\left[\widehat{M}_r\frac{\mathrm{d}\widehat{H}_z^*}{\mathrm{d}r} + \mathrm{j}k\widehat{M}_z\widehat{H}_z^*\right].\end{aligned} \tag{18}$$

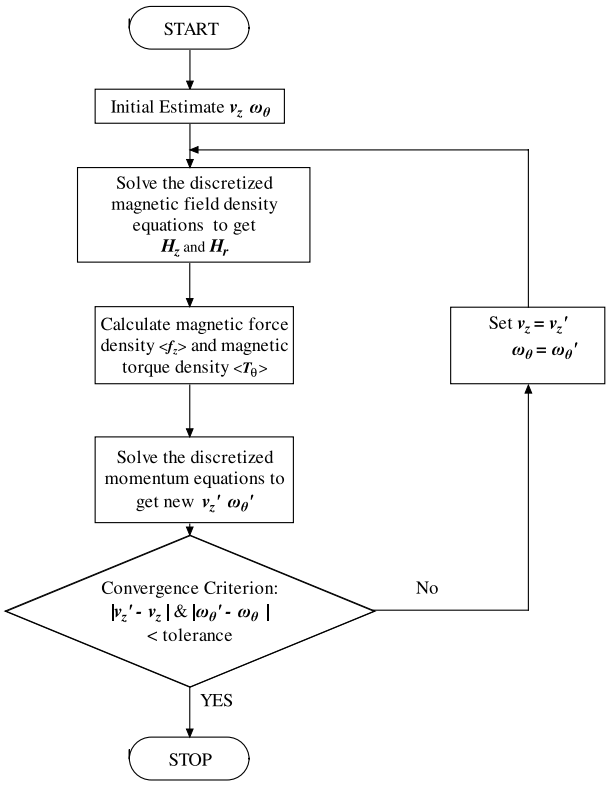

Figure 2. Algorithm flowchart for solving flow velocity, particle spin angular velocity and magnetic field strength.

The torque density inside the ferrofluid is given by [1]

$$\mathbf{T} = \mu_0 (\mathbf{M} \times \mathbf{H}) . \tag{19}$$

The torque has only a θ-directed component, so the time average of torque density is

$$\langle T_\theta \rangle = \tfrac{1}{2}\mu_0 \mathrm{Re}\left[-\widehat{M}_r \widehat{H}_z^* + \widehat{M}_z \widehat{H}_r^*\right]. \tag{20}$$

2.5. Solution method

Equations (6) and (7) are numerically solved by an iterative method with a second-order central-differencing scheme. The flow chart is shown in figure 2. First, initial estimates of $\mathbf{v}$ and $\boldsymbol{\omega}$ are made to calculate magnetic field by using (13); then, force density $\mathbf{f}$ and torque density $\mathbf{T}$ are determined from (18) and (20). After that, new sets of $\mathbf{v}'$ and $\boldsymbol{\omega}'$ are obtained by solving (6) and (7). We compare the new $\mathbf{v}'$ and $\boldsymbol{\omega}'$ with previous values; if the norm of the difference is larger than a preset tolerance, $\mathbf{v}'$ and $\boldsymbol{\omega}'$ become the new estimates, and the iteration continues till the tolerance criterion is met.

2.6. Discretization method

Figure 3 shows the discretization scheme with n unit cells across the radial distance. Within each unit cell, flow velocity, spin velocity and magnetic field values are constant. Discretizing the magnetic field equation (13) in this scheme

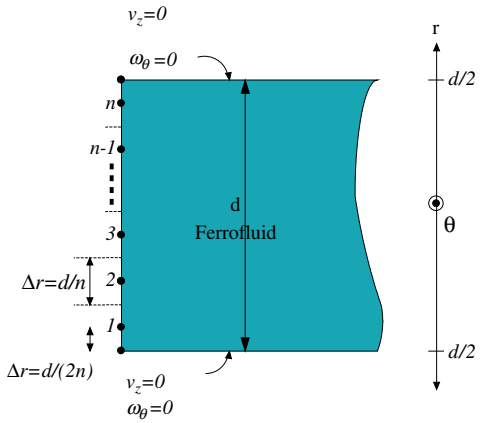

Figure 3. Discretization in the r-direction. Within each unit cell, the flow velocity v_z, spin velocity ω_θ and the z-component of magnetic field are assumed to be constant.

yields

$$\begin{aligned}
\widehat{H}_z(r)\Big|_{r=(i-1)\Delta r+\frac{\Delta r}{2}} &= \widehat{H}_{z,i}, \\
\frac{\mathrm{d}\widehat{H}_z(r)}{\mathrm{d}r}\Big|_{r=(i-1)\Delta r+\frac{\Delta r}{2}} &= \frac{\widehat{H}_{z,i+1} - \widehat{H}_{z,i-1}}{2\Delta r} \\
\frac{\mathrm{d}^2\widehat{H}_z(r)}{\mathrm{d}r^2}\Big|_{r=(i-1)\Delta r+\frac{\Delta r}{2}} &= \frac{\widehat{H}_{z,i+1} + \widehat{H}_{z,i-1} - 2\widehat{H}_{z,i}}{(\Delta r)^2}.
\end{aligned} \tag{21}$$

The discretized equation (13) is of the form

$$a_{H,_{i+1}}\widehat{H}_{z,i+1} + a_{H,_i}\widehat{H}_{z,i} + a_{H,_{i-1}}\widehat{H}_{z,i-1} = 0 \tag{22}$$

where

$$\begin{aligned}
a_{H,i+1} &= \frac{1}{(\Delta r)^2} - \frac{1}{2\Delta r}\cdot\left[1 + \frac{1}{1+C_{i+1}}\left(\frac{\mathrm{d}C}{\mathrm{d}r}\right)_{i+1}\right] \\
a_{H,i} &= -\frac{2}{(\Delta r)^2} + \left[\frac{-\mathrm{j}\,k}{1+C_i}\left(\frac{\mathrm{d}D}{\mathrm{d}r}\right)_i - k^2\right] \\
a_{H,i-1} &= \frac{1}{(\Delta r)^2} + \frac{1}{2\Delta r}\cdot\left[1 + \frac{1}{1+C_{i-1}}\left(\frac{\mathrm{d}C}{\mathrm{d}r}\right)_{i-1}\right].
\end{aligned} \tag{23}$$

Note that C, D, $\mathrm{d}C/\mathrm{d}r$ and $\mathrm{d}D/\mathrm{d}r$ are evaluated numerically using the $\mathbf{v}$ and $\boldsymbol{\omega}$ values from the previous iteration. Similarly, discretizing (6) and (7) gives

$$\begin{aligned}
&m_{v,i+1}v_{z,i+1} + m_{v,i}v_{z,i} + m_{v,i-1}v_{z,i-1} + m_{\omega,i+1}\omega_{\theta,i+1} \\
&\quad + m_{\omega,i}\omega_{\theta,i} + m_{\omega,i-1}\omega_{\theta,i-1} = b_{m,i} \\
&n_{v,i+1}v_{z,i+1} + n_{v,i}v_{z,i} + n_{v,i-1}v_{z,i-1} + n_{\omega,i+1}\omega_{\theta,i+1} + n_{\omega,i}\omega_{\theta,i} \\
&\quad + n_{\omega,i-1}\omega_{\theta,i-1} = b_{n,i}
\end{aligned} \tag{24}$$

where

$$\begin{aligned}
m_{v,i+1} &= (\eta+\zeta)\left[\frac{1}{(\Delta r)^2} + \frac{1}{(2i-1)(\Delta r)^2}\right], \\
m_{v,i} &= -\frac{2(\eta+\zeta)}{(\Delta r)^2} \\
m_{v,i-1} &= (\eta-\zeta)\left[\frac{1}{(\Delta r)^2} + \frac{1}{(2i-1)(\Delta r)^2}\right],
\end{aligned}$$

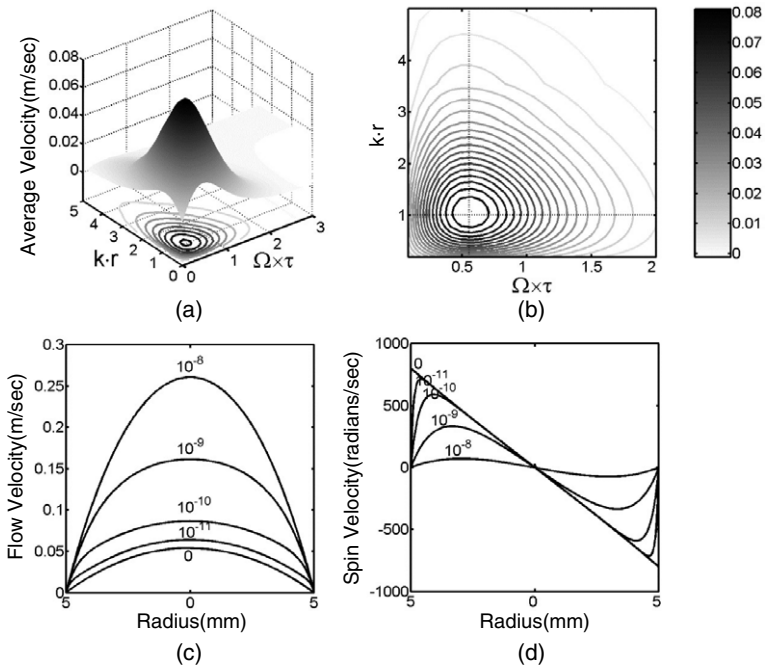

Figure 4. 3D (a) and contour (b) plots of average flow velocity of ferrofluid versus the product of wavenumber and the height of the channel ($k \cdot r$) for various applied magnetic field frequencies. The Brownian relaxation time constant for the nanoparticles (τ), as well as the geometry, determine the pumping peak. Maximum pumping is achieved when the product $k \cdot r$ is approximately unity. Pumping efficiency increases as the applied magnetic field frequency becomes comparable to the reciprocal of the relaxation time constant of magnetic particles in the ferrofluid. The flow velocity (c) and particle spin velocity (d) profiles inside the cylinder for various spin viscosity η' values are also shown. Here $K_s = 8000$ A m^{-1}, height of channel $r = 5$ mm, travelling wave period $\lambda = 2\pi/k = 4$ cm, $\chi_0 = 1.7$, $\tau = 13$ μs, $\eta = 0.006$ kg m^{-1} s^{-1}, $\zeta = 0.000\,81$ kg m^{-1} s^{-1}, $\eta' = 0$, 10^{-11}, 10^{-10}, 10^{-9}, and 10^{-8} kg m^{-1} s^{-1}. Relevant material properties correspond to the EFH1 ferrofluid (Ferrotec, Nashua, NH) used in actual experiments.

$$
\begin{aligned}
&m_{\omega,i+1} = \frac{\zeta}{\Delta r} \\
&m_{\omega,i} = \frac{2\zeta}{(i-\frac{1}{2})\Delta r}, \qquad m_{\omega,i-1} = -\frac{\zeta}{\Delta r}, \\
&b_{m,i} = -\langle f_z \rangle_i + \frac{\mathrm{d}p}{\mathrm{d}z} \\
&n_{v,i+1} = -\frac{\zeta}{\Delta r}, \qquad n_{v,i} = 0, \qquad n_{v,i-1} = \frac{\zeta}{\Delta r} \\
&n_{\omega,i+1} = \eta' \left[\frac{1}{(\Delta r)^2} + \frac{1}{(2i-1)(\Delta r)^2} \right], \\
&n_{\omega,i} = \frac{2\eta'}{(\Delta r)^2} - \eta' \frac{1}{\left[(i-\frac{1}{2})(\Delta r)\right]^2} \\
&n_{\omega,i-1} = \eta' \left[\frac{1}{(\Delta r)^2} - \frac{1}{(2i-1)(\Delta r)^2} \right], \\
&b_{n,i} = -\langle T_\theta \rangle_i .
\end{aligned}
\tag{25}
$$

2.7. Simulation results

In the real physical system, the spin viscosity η' is typically very small but nonzero. The ferrofluid flow velocity and magnetic particle spin profiles inside a cylinder are shown in figure 4. Note that non-slip boundary conditions for both $\mathbf{v}$ and $\boldsymbol{\omega}$ are satisfied, except when $\eta' = 0$. To obtain the ferrofluid flow and spin profiles in the small spin viscosity case, we simply set the spin viscosity $\eta' = 0$, which reduces the governing equations (6) and (7) to a second order system. Corresponding results are also shown in figure 4. The parameters in figure 4 are chosen to correspond to those of a commercially available, EFH1 oil-based ferrofluid (Ferrotec, Nashua, NH). Average flow velocities for various travelling wave periods and magnetic field frequencies also appear in figure 4. The flow velocity is strongly dependent on the travelling wave period. Maximum flow velocity is achieved when the product of the excitation wavenumber and radius of the ferrofluid cylinder approaches unity. Once geometric dimensions are chosen, the flow velocity can be precisely controlled by the applied magnetic field frequency. As shown in figure 4, maximum flow velocity is achieved when the applied magnetic field frequency is comparable to the reciprocal of the relaxation time constant of magnetic particles inside the ferrofluid. Interestingly, as η' is chosen smaller, the maximum pumping peak shifts from $\Omega \cdot \tau = 1$ to $\Omega \cdot \tau = 0.5$.

3. Initial experimental results

An indirect way to quantify ferrofluid pumping is to measure the pressure difference introduced in the fluid by the action of the travelling wave excitation. This measurement in the macro-scale can be accomplished using a U-tube set-up (as shown in figure 5), where change in the height of a fluid column would be directly related to the pumping pressure. The modelling approach introduced above can also be used to determine the pumping pressure, the backpressure that would be required to stop ferrofluid flow, which provides one mechanism of comparing experimental measurements to

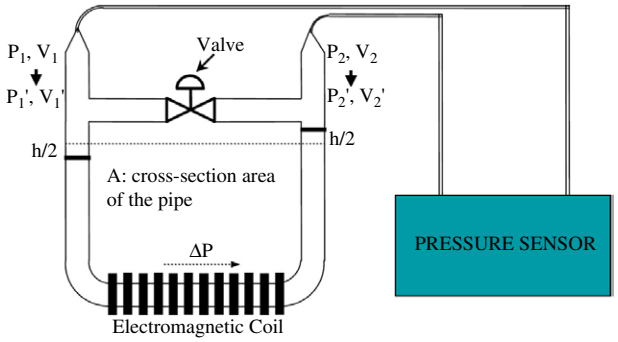

Figure 5. Schematic diagram of the experimental set-up used to determine the pumping pressure acting on the ferrofluid due to the travelling wave excitation within the electromagnetic coils. The electromagnetic coil windings simulate a travelling magnetic field.

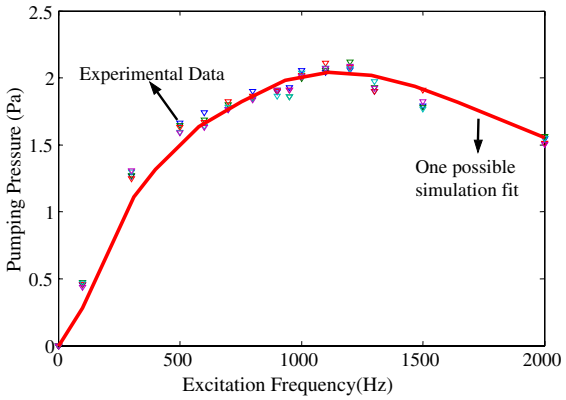

Figure 6. Pumping pressure versus applied excitation frequency as measured using the U-tube set-up at 10 A of current amplitude. The corresponding magnetic field amplitude just inside the windings is about 8000 A m^{-1}.

theoretical simulations. In figure 5, electrical current is passed through the coils in a two-phase configuration that is set up to result in a travelling magnetic field with known fundamental amplitude. Figure 6 shows initial experimental data obtained using the set-up of figure 5. The peak of the pumping in figure 6 occurs around 1.2 kHz, corresponding to a time constant of around 100 μs. Based on figure 6, this time constant predicts an effective particle size of around 26 nm. Figure 6 also depicts a simulation fit to data for this particle size, in the case when spin viscosity is zero and only 2% of the entire particle ensemble within the ferrofluid has this effective diameter (i.e., a small percentage of the particles forming doublets or triplets with the effective average diameter of about 26 nm). A higher particle percentage would correspond to a higher measured pressure. The power amplifiers used to obtain the data of figure 6 are not powerful enough to drive the high inductive load of the coils at high frequencies (up to 100 kHz) and currents. Miniaturizing the entire set-up would dramatically reduce the inductance of the excitation coils while still maintaining detectable pressure changes. This observation, coupled with the theoretical work outlined above, motivates the creation of ferro-microfluidic devices as described in the next section.

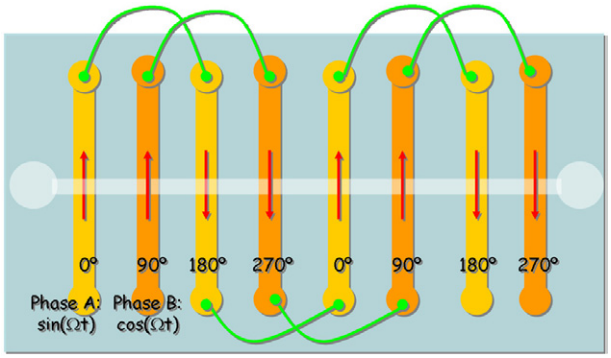

Figure 7. Top schematic view of the prototype micro-state device. A magnetic field travelling from right to left under a microfluidic channel (depicted as the horizontal channel over the electrodes) can be created via an electrode pattern in which a sinusoidal electrical current is applied in increasing increments of 90° phase shifts to each succeeding electrode from left to right. This excitation pattern can be achieved using two input phases.

4. Micro-scale devices

Figure 7 introduces the basic microfluidic device concept. For simplicity, the prototype devices are currently fabricated using a single layer of etched electrode patterns on thermal-clad insulated metal substrate (IMS) printed circuit board (PCB). The electrodes are wire bonded in a pattern that results in a 90° current phase difference between each adjacent electrode, as shown in figure 7. The resulting fundamental component of the magnetic field over the wires is a travelling wave, just like the travelling excitation over the stator surface in an electric motor. The microfluidic channel over the excitation electrodes is created using soft lithography [12].

4.1. MEMS device simulation

A numerical analysis, similar to the one described in section 2, has been conducted for the planar geometry of the micro-ferrofluidic devices, and the details have been documented [13]. Figure 8 depicts the theoretical and experimental set-up in Cartesian coordinates. A current sheet travelling to the right just outside the flow channel creates a travelling magnetic field that interacts with and pumps the ferrofluid. The pumping action of the travelling field imparts both linear and angular momentum to the ferrofluid, resulting in linear and spin velocity profiles across the channel. Typically, the linear and spin velocities are assumed to be zero at the channel interior boundaries (no-slip conditions). The simulation results are shown in figure 9. Note that

(i) maximum flow velocity is achieved when the product of the excitation wavenumber and the height of the ferrofluid channel approaches unity, and
(ii) the excitation frequency is given by the reciprocal of the Brownian relaxation time constant of the magnetic nanoparticles.

The implication of (i) above is that, once the channel height is chosen for a specific application (to accommodate a particular cell size in a lab-on-a-chip device, for instance), the optimum separation between the excitation windings is also

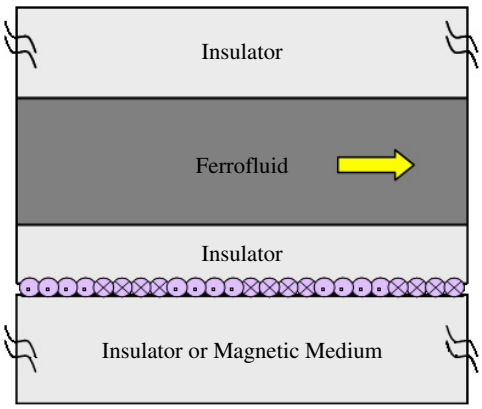

Figure 8. The geometrical set-up for Cartesian coordinates.

set. In the context of a micro-scale device, finding (ii) means that, given a specific particle size composition in the ferrofluid, the driving circuit must be capable of providing relatively high currents at the corresponding optimum pumping frequency.

4.2. Device fabrication

A significant temperature rise within the microchannel would adversely affect the pumping dynamics by reducing the overall magnetization of the ferrofluid. in that regard, the electrode substrate must allow good thermal contact between a heat sink and the copper electrodes. We have chosen a thermal-clad, insulated metal substrate (IMS) printed circuit board (PCB) as the starting substrate, due mainly to its superior heat dissipation characteristics; we have also tried a common glass-epoxy PCB for comparison. Figure 10 depicts the process flow and an initial prototype of the MEMS ferrofluidic device designed based on previous numerical analysis. The fabrication process is comprised of two parts: copper electrodes fabricated on the thermal-clad IMS—steps (a)–(f)—and ferrofluid microfluidic channels realized by soft lithography—steps (g)–(k). In this section, fabrication steps shown in figure 10 are discussed in detail.

(a) Substrates. Two kinds of substrates are used in this process for the purposes of comparison. One of them is the common PC board constructed of $1/16''$ glass epoxy with a 35 μm thick copper layer on the top side; the other is a commercial thermal-clad IMS, chosen for its superior heat conduction capability, mechanical robustness and low cost. The IMS printed circuit board used in this study (Bergquist T-clad) is comprised of three layers: 35 μm thick copper for the circuit layer, 75 μm of dielectric layer with minimum thermal resistance, and a 1.6 mm thick aluminium base layer for easy heat removal.

(b) SU-8 photoresist and Omnicoat spin-on. Commonly used photoresists, such as Shipley 1813, often peel off during the high temperature wet etching of copper. Hence, SU-8 50 negative photoresist (Microchem, Newton, MA) is used in this process as a durable wet etching mask to pattern the copper electrodes. To achieve 30 μm thick SU-8, approximately 1 ml of SU-8 per inch of substrate diameter is dispensed; spread cycle, ramp to 500 rpm at 100 rpm s^{-1} acceleration and hold for 5–10 s; spin cycle, ramp to final spin speed 3250 rpm at an acceleration of 300 rpm s^{-1} and hold for a total of 30 s. A thin layer (17 nm) of Omnicoat (Microchem, Newton, MA) between the copper and the photoresist improves adhesion and facilitates the easy removal of the 30 μm thick SU-8 after patterning.

(c) SU-8 photoresist patterning. After the soft bake step, SU-8 photoresist is exposed under an EVG 620 mask aligner, post-baked, and developed to open the etching windows over the copper layer. Before wet etching, the Omnicoat layer in the etching windows is removed by a developer (Microposit MF 319, Shipley, Marlborough, MA).

(d) Copper layer wet etching. Ferric chloride solution at 60 °C is used to etch copper. The typical copper electrode dimensions are 240 μm in width and 2.5 cm in length, with 80 μm spacing between two electrodes. In order to get a uniform etch rate for all electrodes, constant agitation during etching is required.

(e) SU-8 and Omnicoat removal. The substrate is immersed into Remover PG (Microchem, Newton, MA) at 80 °C for 30 s. The resulting copper surface is clean and ready for wire bonding.

(f) Wire bonding and PDMS spin-on. The copper electrodes are connected by wire bonds to form a two-phase travelling magnetic field when excited by sinusoidal currents. in order to accommodate high electric currents, multiple aluminium wire bonds are performed on each connection pad using a Westbond 7400E bonder. Afterwards, the wire bonds are encapsulated by epoxy for mechanical robustness. A 50 μm thick layer of the elastomer polydimethylsiloxane (PDMS, Sylgard 184, from Dow Corning, Midland, MI) is spun onto the copper electrodes and cured at 80 °C for 2 h. To achieve 50 μm thick PDMS, approximately 1 ml of PDMS per inch of substrate diameter is dispensed; spread cycle, ramp to 500 rpm at 100 rpm s^{-1} acceleration and hold for 5–10 s; spin cycle, ramp to final spin speed 1500 rpm at an acceleration of 300 rpm s^{-1} and hold for a total of 50 s. The PDMS layer insulates the electrodes from the microfluidic channel that will later be attached to the IMS.

(g) Substrate for SU-8 master. A $3''$ silicon wafer (single-side polished) is used as the SU-8 mould substrate. Piranha cleaning (3:1 H_2SO_4:H_2O_2) and a dehydration bake of the substrate improves the eventual adhesion of SU-8.

(h) SU-8 photoresist spin-on. After the dehydration bake, SU-8 photoresist is spun onto the silicon substrate. To achieve 100 μM thick SU-8, approximately 1 ml of SU-8 per inch of substrate diameter is dispensed; spread cycle, ramp to 500 rpm at 100 rpm s^{-1} acceleration and hold for 5–10 s; spin cycle, ramp to final spin speed 1250 rpm at an acceleration of 300 rpm s^{-1} and hold for a total of 30 s. The thickness of SU-8 determines the PDMS microfluidic channel height. A DEKTAK profiler is used to confirm the thickness of the SU-8 photoresist.

(i) SU-8 photoresist patterning. After a soft bake, SU-8 photoresist is exposed under an EVG 620 mask aligner, post-baked, and developed to create the final SU-8 master for the microfluidic channel.

(j) Casting the PDMS mould. 10:1 ratio PDMS pre-polymer base and curing agent are mixed and degassed in a vacuum desiccator. Before the PDMS mixture is poured, the SU-8 master is silanized for five minutes with

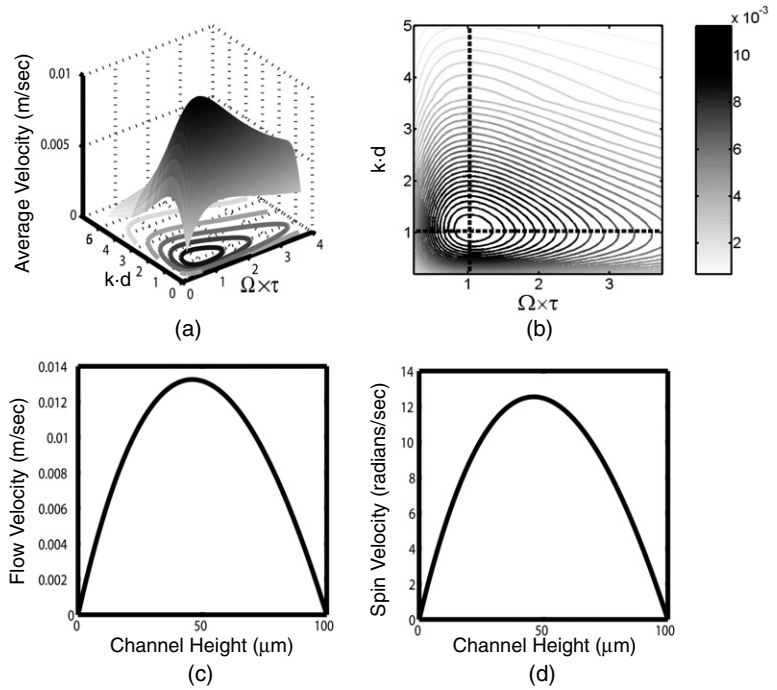

Figure 9. 3D (a) and contour (b) plots of average flow velocity of ferrofluid versus the product of wavenumber and the height of the channel ($k \cdot d$) for various applied magnetic field frequencies. The Brownian relaxation time constant for the nanoparticles (τ), as well as the geometry, determine the pumping peak. The flow velocity (c) and particle spin velocity (d) profiles across the height of the microchannel are also shown. Here, $K_s = 10\,000$ A m^{-1}, height of channel $d = 100$ μm, travelling wave period $\lambda = 2\pi/k = 1.26$ mm, $\chi_0 = 1.17$, $\tau = 3.75$ μs, $\eta = 0.0045$ kg m^{-1} s^{-1}, $\zeta = 0.000\,39$ kg m^{-1} s^{-1}, and $\eta' = 10^{-9}$ kg m^{-1} s^{-1}. Relevant material properties correspond to the EMG 700 series ferrofluid (Ferrotec, Nashua, NH) used in actual experiments. The excitation frequency is 42 kHz, chosen to correspond to maximum pumping given τ.

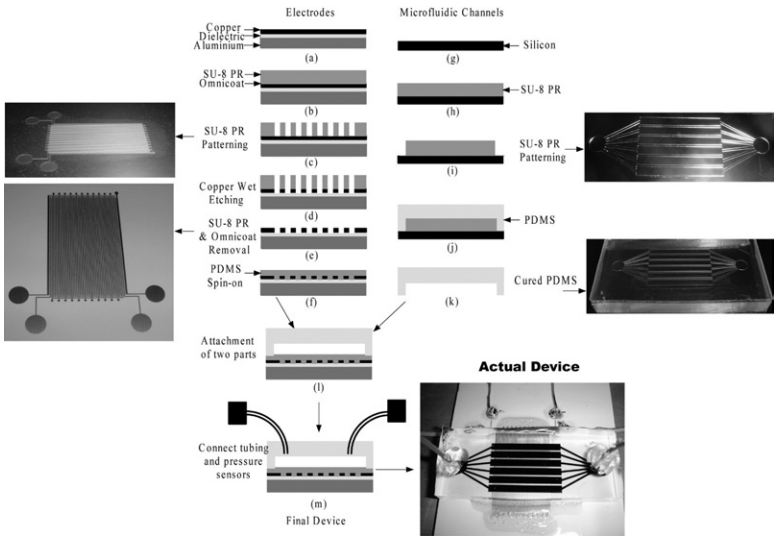

Figure 10. Fabrication process steps for the MEMS ferrofluidic device. Pictures of the intermediate and completed device are also shown.

tetramethylchlorosilane (TMCS) from Aldrich. Once poured onto the silanized master, the mixture is again degassed and cured at 80 °C in an oven for 2 h.

(k) PDMS removal. Once cured, the PDMS microfluidic device is easily peeled off from the silanized SU-8 master, and fluidic connection holes are punched in. the SU-8 master can be reused many times to create more PDMS devices.

(l) Attachment of the microfluidic device to IMS. Treating the PDMS surfaces on both the microfluidic component and the IMS with plasma (in a plasma cleaner chamber from Harrick Scientific, Pleasantville, NY) at 84 mTorr O_2 partial pressure with 18 W power for one minute renders them hydrophilic and incorporates oxygen onto the surface; this procedure yields a hydrophilic PDMS surface, and the PDMS on both device

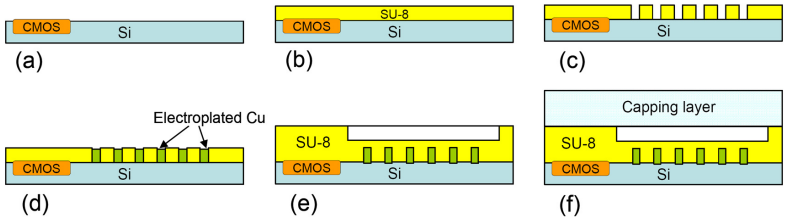

Figure 11. A simple fabrication scheme for integrated, ferrofluid-based pathogen detectors (copper electroplated seed layer not shown).

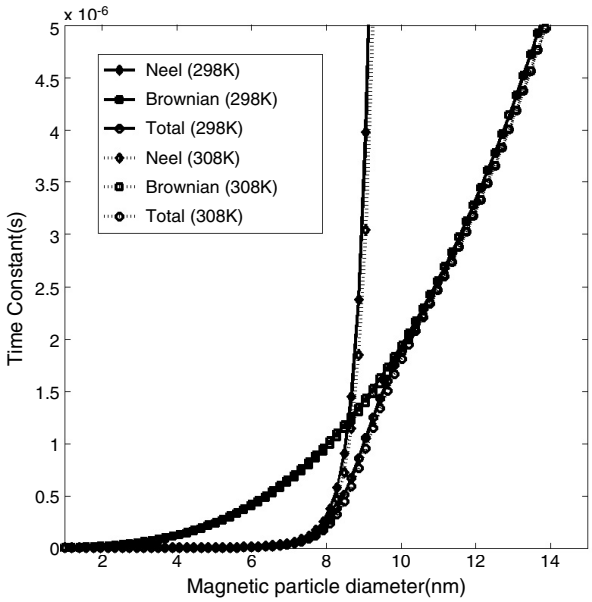

Figure 12. Time constant versus magnetic particle diameter for EMG 700 series ferrofluid. The viscosity is 4.5 cP; the anisotropy constant is 78 000 J m^{-3}.

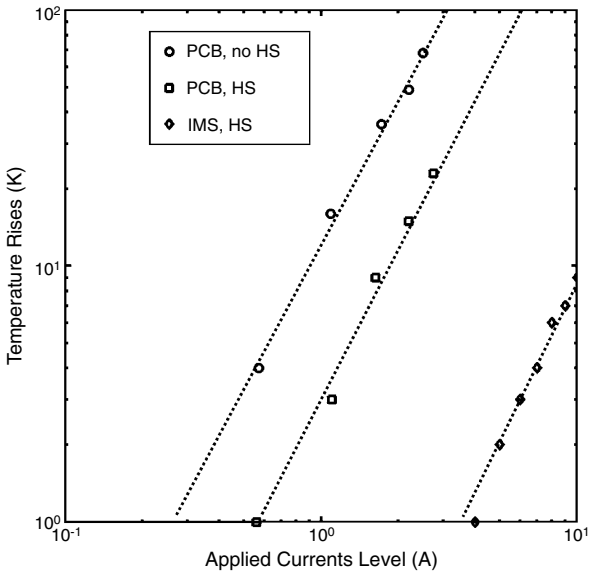

Figure 13. Temperature rise versus applied current level (peak-to-peak amplitude) for two kinds of substrates. PCB represents the commonly used PC boards with copper layer on glass epoxy; IMS is the thermal-clad insulated metal substrate. HS stands for 'heat sink', which in our experiment is a 6 inch by 6 inch, 2 cm thick aluminium piece. Temperature rise is measured using a thermocouple close to the copper electrodes once an AC current (at 1 kHz) has been applied for 6 min to reach steady state. The dashed lines in the plot have a slope of 2, indicating that the heating is proportional to the square of the current amplitude, as expected.

components attach strongly when contacted. This attachment is presumably facilitated via oxygen bonds between silanol groups [14], formed on the PDMS surface by the plasma. Baking the composite structure at 65 °C for about half an hour enhances the attachment further.

(m) Final assembly. Attaching tubing and pressure sensors to the microfluidic device completes the fabrication process.

The actual device shown in figure 10 contains EMG 700 series water-based ferrofluid (Ferrotec, Nashua, NH) in its microfluidic channels. The fabrication scheme outlined above is adopted at this stage because it enables rapid and cheap prototyping during the device optimization stage. Eventually, a fully integrated device will be fabricated on silicon substrates. One possible fabrication scheme would involve first sending the silicon wafers to a CMOS foundry for the fabrication of the electronic controller and sensor components (see figure 11(a)). Subsequently, the CMOS area will be protected via SU-8 (figure 11(b)), which will then be patterned into electroplating moulds at appropriate locations in the dies in order to create thick copper electrodes (figures 11(c) and (d)). The ferrofluid channel over the electrodes may be formed by patterning a second layer of SU-8 (figure 11(e)), and the top of the channel may be capped (figure 11(f)) via a low temperature bonding process (PDMS, glass or silicon wafers may be used to cover the channels).

4.3. Experimental results and discussion

The first performance issue to be addressed is the ability of the substrate to dissipate heat. We tested the thermal performance of ferrofluid micropumps fabricated using glass epoxy and IMS based PCBs; the results are depicted in figure 13. It is clear that the temperature rise of the liquid within the microfluidic channel of the glass epoxy PC board is much larger than that of the IMS-based device. An external aluminium heat sink helps the glass epoxy PCB dissipate heat faster, but the insulated metal substrate is still a much better choice for this application.

Figure 14 shows a sample TEM image and overall particle size distribution of the EMG 700 ferrofluid. The Brownian relaxation time constant (τ) of a ferrofluid is given by $4\pi r^3 \eta_0 / kT$, where r is the overall effective radius of the nanoparticles (a mode of 6.5 nm for EMG 700), η_0 is the

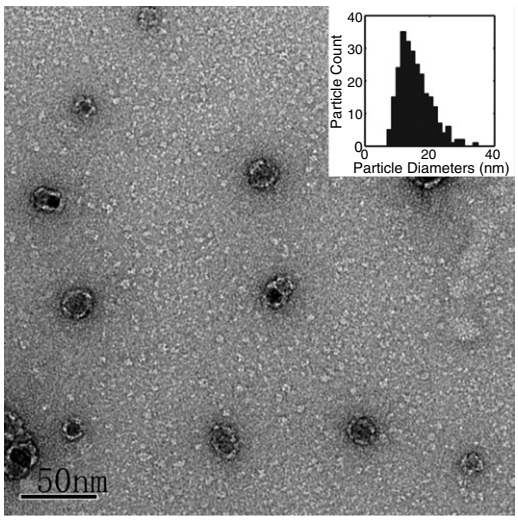

Figure 14. A sample TEM image of EMG 700 series water-based ferrofluid and the overall particle size distribution. The particles have log-normal distribution, as expected.

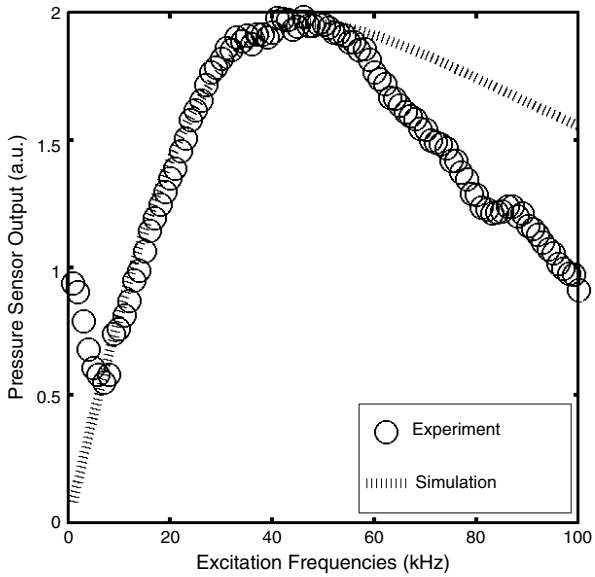

Figure 15. Experimental results and a theoretical fit for the pumping characteristics of an EMG 700 series water-based ferrofluid in the MEMS ferrofluidic device.

viscosity of liquid (4.5 cP), k is the Boltzmann constant, and T is the temperature (300 K) [1]. Based on the discussion in the theory section above, the ferrofluid pumping peak frequency is therefore expected to be around 42 kHz. Figure 15 compares the experimental ferrofluid pumping characteristics of the micropump to the predictions of the theory [15]. Since static pumping pressure, and not fluid velocity, is measured, the numerical models are run iteratively to determine the pressure differential that results in stopped flow. The only fit parameter in the simulation is the magnitude scaling of the signal; the uncertainty arises from the difficulty of absolute pressure calibration of the sensors. Notice, however, that the pumping peak location is where it is expected. The experimental pumping curve depicted in figure 15 deviates in at least two ways from the simple theory that assumes a monodisperse suspension of particles and constant environmental conditions. First, at relatively low frequencies, there is a minor pumping peak associated with a certain fraction of particles forming small agglomerates in the presence of the applied fields. The frequency of this minor pumping peak (around 1 kHz) indicates an effective hydrodynamic radius about three times that of the median. Second, there is a clear discrepancy between experiment and simple theory as the excitation frequency is increased beyond the main pumping peak. One possible explanation for this discrepancy is eddy-currents induced in the aluminium layer of the IMS, which slightly reduce the effective magnetic field that couples to the main flow channel. At higher frequencies, eddy-currents effectively decrease the magnetic field inside the ferrofluid pumping channel, resulting in reduced pumping. Next generation devices will feature fully insulating, thermally highly conductive PCB substrates to alleviate this phenomenon.

5. Pathogen detection scheme

5.1. Sensing principle

In our paper, the dependence of the optimal pumping peak on the Brownian relaxation time constant suggests an effective scheme for pathogen detection. When target molecules or pathogens bind to the surface of a functionalized magnetic nanoparticle within a ferrofluid, the particle's overall hydrodynamic volume increases, causing a corresponding rise in its Brownian relaxation time constant. Consequently, with enough particles bound to antigens, the optimum pumping frequency will shift towards a lower value. A quick sweep of pumping pressure versus excitation frequency, conducted both before and after the binding, will reveal the peak shift and signal the presence of the antigen.

There are two mechanisms by which the magnetization of a colloidal ferrofluid can relax after the applied field has been changed [1]. In the first mechanism, the relaxation occurs by particle rotation in the liquid. In the second mechanism the relaxation is due to rotation of the magnetic vector within the particle. The first mechanism is characterized by a Brownian rotational time constant of $\tau_B = 3V\eta_0/kT$, where V is the particle volume, η_0 is the viscosity of the carrier medium, k is the Boltzmann constant and T is the temperature in kelvin. The second relaxation mechanism is characterized by a Néel time constant $\tau_N = (1/f_0)\exp(KV/kT)$, where f_0 is a frequency having the approximate value of 10^9 Hz. K is the anisotropy constant of the material.

When $\tau_N \ll \tau_B$, relaxation occurs by the Néel Mechanism; when $\tau_B \ll \tau_N$, relaxation occurs by the Brownian mechanism, i.e.

$$\frac{1}{\tau} = \frac{1}{\tau_B} + \frac{1}{\tau_N}.$$

Figure 12 shows the relationship between the overall time constant and magnetic particle diameter. For particle diameters larger than 10 nm, the Brownian relaxation mechanism determines the total relaxation time constant.

In this approach, a ferrofluid with non-functionalized magnetic particles (e.g. 10 nm average overall hydrodynamic diameter) will be divided into two parts. The magnetic

particles in one of them will be coated with the specific receptors (e.g. typical 10–20 nm antibodies); the effective hydrodynamic diameter of the coated nanoparticles will then be 20–30 nm. The ferrofluid produced by mixing these two parts has equal amounts of 10 and 30 nm (assuming 20 nm antibodies are used) effective hydrodynamic diameter particles, which corresponds to two different pumping peaks. Inevitably, there are smaller diameter particles (<10 nm) which relax through the Néel mechanism. One can carefully engineer the ferrofluids (e.g. change the viscosity, change the mean particle diameter, etc) so that the great majority of the magnetic particles are Brownian particles and the observed effect only comes from the Brownian relaxation mechanism.

For both 10 and 30 nm diameter particles, the Brownian relaxation mechanism dominates (figure 12). Only the Brownian particles contribute to the observed effect. In our experiment, according to figure 13, the maximum temperature rise of ferrofluids upon applying the electric current to the copper wires is approximately 10 K (corresponding to the worst-case scenario of large currents applied for a long time period—6 min in this case), that is a 3.4% change from room temperature. As shown in figure 13, this amount of temperature change results in approximately 3% change in Néel, Brownian and total relaxation time. At room temperature (298 K), particles with diameters less than 8.6 nm can be considered as Néel particles; when the temperature rises to 308 K, particles with a diameter less than 8.8 nm can be considered as Néel particles. Considering that under 1% of particles have a diameter of 8.6 nm or less in the ferrofluid (EMG 700 series from Ferrotec, Nashua, NH), the 10 K temperature rise has minimal effect on the Brownian particles' pumping. Furthermore, this issue can be eliminated with better engineered ferrofluids (less polydisperse) and more efficient cooling schemes to keep ferrofluids' temperature constant in the future.

Additionally, the pathogen detection scheme takes peak frequency readings both before and after the sample is introduced. Without the sample, when currents are applied, the temperature rise, if any, will be the same (to first order and assuming insignificant changes to the thermal capacity of the ferrofluid) as that of the ferrofluid/sample mixture.

The surface of the magnetic nanoparticles can be chemically modified to immobilize a specific antibody. For example, in order to detect *E. coli* O157, the magnetic nanoparticle surfaces can be modified to immobilize mAbs [18]. Here, an amine-functionalized group formed on the nanoparticle surfaces facilitates conjugation of antibodies against *E. coli* O157.

For small molecules that bind to the functionalized nanoparticles, as long as the overall hydrodynamic diameter is still small so that the thermal energy at room temperature can overcome the gravitational energy of the particles, the colloidal particle suspension is stable [1]. Because all nanoparticles contributing to pumping are Brownian, the relative shift in optimal excitation frequency can be used to measure the binding affinity and target molecule size. In general, there will always be a viscosity difference between the ferrofluid in the pathogen sensor and the input liquid sample to be tested (whether the sample is saliva, blood or potentially contaminated water). Mixing the sample with the ferrofluid will alter its overall viscosity. Recall that the Brownian time constant is proportional to viscosity as well. Hence, if the change in a single pumping peak's location is used for pathogen detection, even a pathogen-free sample will inevitably give spurious results and false positives.

We propose a solution to the viscosity mismatch issue by using multiple pumping peaks for detection. In this approach, a ferrofluid with non-functionalized magnetic particles (e.g., 10 nm average overall hydrodynamic diameter) will be divided equally into two parts. The magnetic particles in one will be coated with specific receptors (e.g., typical 10–20 nm antibodies), yielding coated nanoparticles with an effective average hydrodynamic diameter of 30 nm (assuming 20 nm antibodies). The ferrofluid produced by mixing these two parts will have a given ratio of 10 and 30 nm particles, resulting in two different pumping peaks. If the pathogen is not present, both pumping peaks will shift in frequency by exactly the same percentage, corresponding to the effect of the viscosity change alone. If pathogen molecules are present and bind to the larger particles, then the relative shift in frequency will be different for the two peaks. By using one of the Brownian relaxation peaks as a control, this approach is insensitive to changes in viscosity that occur after the sample introduction. The double-peak detection scheme is illustrated in figure 16; for simplicity, viscosity, temperature or relative volume concentration changes that will occur after the sample introduction have not been shown. By the same token, the double-peak detection scheme introduced above is also insensitive to slight temperature changes (Brownian relaxation is inversely proportional with temperature). Such temperature changes would normally occur due to mismatches in the initial temperatures of the ferrofluid and the sample liquid, as well as minor heating of the ferrofluid by the excitation coils during measurements.

We anticipate that the excellent sensitivity of the state-of-the-art, integrated MEMS pressure sensors [19] that will be used in conjunction with the micro-ferrofluidic device introduced here will enable the realization of a sensitive pathogen detector chip. For small molecules, the exact sensitivity for a given pathogen will depend on the binding affinity of the receptor molecule and the steady-state solubility of the target pathogen within the ferrofluid. Let us assume that every small target molecule binds eventually to one functionalized nanoparticle (low pathogen concentration and high affinity limit), and the frequency detection limit $\Delta f_0/f_0$ is about 1%, which is a realistic estimate based on our experiments (Δf_0 is the shift in the optimal pumping frequency, and f_0 is the optimal pumping frequency position). For the functionalized nanoparticles (30 nm overall diameter) binding to small target molecules (1 nm diameter) in figure 16, the smallest detectable frequency shift Δf_0 will then be 36 Hz. Considering an integrated MEMS flow or pressure sensor [19] that can measure down to 70 nm s^{-1} flow rate (corresponding to 31 μPa pressure), a ferrofluid with the concentration of 10^9 particles ml^{-1} is more than enough to produce a measurable flow or pressure signal according to the simulation results. In this case, 36 Hz frequency shift corresponds to 1% of the total functionalized nanoparticles experiencing size changes. Therefore, the detection limit is in this case is 10^7 molecules ml^{-1}.

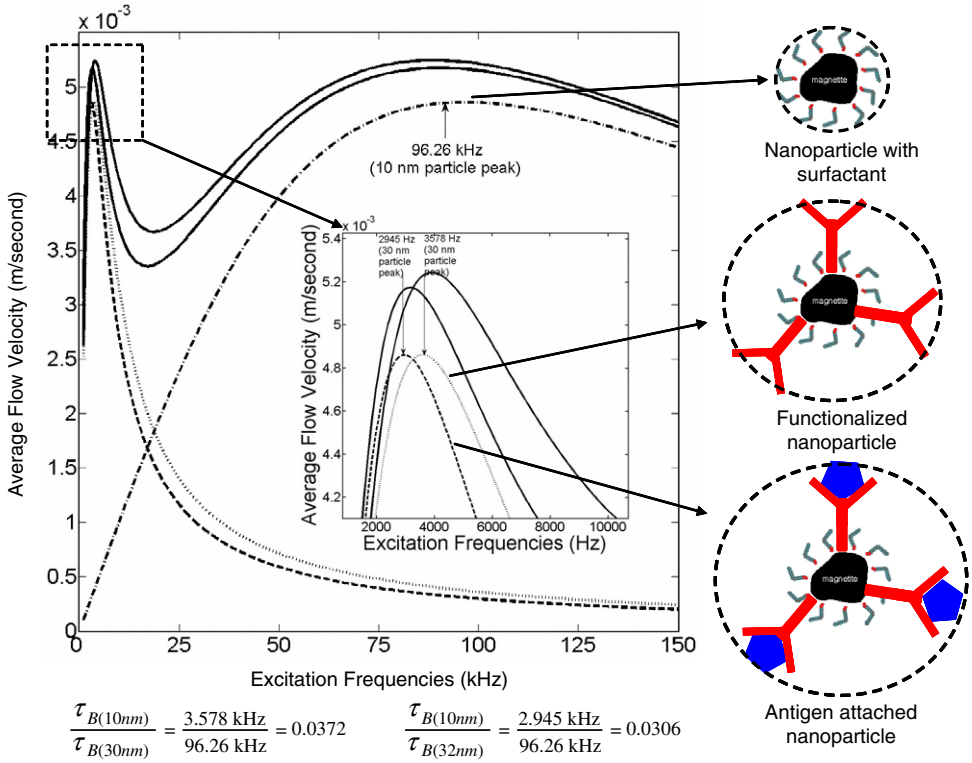

Figure 16. A change in optimal pumping frequency (close to 1 kHz) occurs when functionalized 30 nm diameter particles bind to 1 nm analytes, effectively increasing their hydrodynamic diameter to 32 nm. Non-functionalized 10 nm diameter particles are added as a control to eliminate the viscosity and temperature change effects. $K_s = 10$ kA m^{-1}, height of channel $d = 100$ μm, travelling wave period $\lambda = 2\pi/k = 0.628$ mm, initial susceptibility $\chi_0 = 1.17$, dynamic viscosity $\eta = 0.0045$ kg m^{-1} s^{-1}, vortex viscosity $\zeta = 0.000\,395$ kg m^{-1} s^{-1}, shear coefficient of spin viscosity $\eta' = 10^{-9}$ kg m^{-1} s^{-1}. In this calculation, there are equal numbers of 10 and 30 nm particles in the ferrofluid. Solid curves in the figure correspond to the overall pumping; dashed curves correspond to the individual pumping contributions from 10/30 nm particles before sample addition and from 10/32 nm particles after sample addition. This figure does not incorporate viscosity or temperature changes.

When it comes to detecting viruses, bacteria and cells using ferrohydrodynamic pumping, the situation is different. Bacteria, for instance, have thousands of identical epitopes on their surfaces [21], where functionalized magnetic nanoparticles will attach and become immobilized, effectively not contributing to pumping. Consequently, one of the pumping peaks corresponding to the functionalized particles in our two-peak detection scheme will go down significantly in amplitude (compared to the peak from the unbound, smaller 10 nm particles), signalling attachment of the functionalized nanoparticles. Any shifts in the frequency peaks may then be used to subtract out the effects of viscosity and temperature changes in the ferrofluid/sample mixture. The exact sensitivity in this case will be species dependent, and will vary strongly based on how many binding sites each cell or virus presents to the surrounding ferrofluid. The amplitude (flow velocity or pressure) resolution determines the detection limit for micro-organisms. As a conservative estimate on detection sensitivity, assume that on average 5000 functionalized nanoparticles bind to one micro-organism, and a root-mean-square noise level of 10 nm s^{-1} [19] is present in flow velocity measurements. Considering a target signal-to-noise ratio of 5, the smallest detectable amplitude change becomes 50 nm s^{-1}. For a ferrofluid with a concentration of 10^9 particles ml^{-1}, simulations show that 50 nm s^{-1} amplitude change corresponds to 10% of the total functionalized nanoparticles not contributing to ferrofluid pumping. Therefore, the detection limit is approximately 2×10^4 micro-organisms ml^{-1}, and the corresponding bacteria detection limit for our 1 μl ferrofluidic biosensor is 20 micro-organisms.

5.2. Advantages over existing sensors

The pathogen sensing scheme introduced in this section involves a novel ferrohydrodynamic pumping scheme based on travelling magnetic fields. The pumping scheme is scalable, and in particular can be miniaturized very effectively to microfluidic dimensions. Here, some of the advantages of this biological sensing scheme over existing, miniaturized pathogen detectors are considered.

5.2.1. Nonmagnetic sensors. Surface plasmon resonance (SPR) [22, 23] is a popular biosensing scheme. The SPR optical biosensor monitors the change in the reflective index of a metal–dielectric surface at a fixed angle, enabling a real-time detection of antibody–antigen binding. A major disadvantage of SPR for biosensor applications is that low concentrations (less than 10^8 cells ml^{-1}) or low molecular mass analytes may not be detected easily. In an enzyme

linked immunosorbent assay (ELISA) [24] antigen molecules are captured on a substrate surface through immobilized antibodies. The procedure uses an antibody-labelled enzyme that attaches to the substrate only in the presence of the target antigen. The enzyme is subsequently used to produce a colour change in a given solution, signalling the presence of bound antigen on the substrate surface. ELISA has high sensitivity ($\sim 10^5$ cells ml^{-1}) but requires long incubation times (hours). The ferrofluidic pathogen detector introduced here is expected to detect the presence of targets within minutes.

Electrochemical sensors [25] including potentiometric [26], amperometric [27] and conductometric [28] biosensors are based on a bio-interaction process, during which charge carriers are consumed or generated to produce an electrochemical signal; this, in turn, can be measured by an electrochemical detector. Electrochemical biosensors are highly sensitive ($\sim 10^3$ cells ml^{-1}) and amenable to miniaturization, but they only work when a biological reaction involves a charge-exchange process.

Resonant cantilever sensors [20, 29] work by detecting a small shift in their fundamental resonance frequency when the mass of the resonant beam is increased slightly as pathogens attach to its surface. Their sensitivities are usually on the order of 10^6 cells ml^{-1}. Unlike the resonant sensor, the ferrofluidic pathogen detector requires no mechanically moving parts; it is more reliable and easier to handle; and it works in a water medium, thereby avoiding shortcomings of the cantilever resonance-based schemes, such as complicated drying procedures, humidity control, complicated fabrication schemes to control the residual stress on a cantilever, and atmospheric control for stable resonance frequencies over time. The ferrofluidic approach will presumably result in much better preservation of functionality of the receptors that coat the particle surfaces, because receptors are kept in their water-based biological environment, as opposed to in air. Due to the very large surface area/volume ratio of the nanoparticles, a very large array of receptors can be presented to the pathogens, and virtually all pathogens, especially in minute concentrations, will be bound, increasing the sensitivity enormously. This is a major advantage compared to all other sensing schemes. In contrast, the cantilever approach (resonant or non-resonant [20]) presents a relatively small surface area to the pathogens, and only a minuscule fraction of the pathogens that reside inside the microfluidic channel volume actually bind to the cantilever surface in reasonable timescales (i.e., the process is highly diffusion limited).

Other sensor schemes [30] involve the attachment of fluorescent tags to pathogen targets and their subsequent optical detection. One problem with fluorescence-based sensors is that their performance depends on the optical properties of their samples; a pathogen sensor designed to analyse blood is not necessarily suitable for analysing water samples. Moreover, a fluorescent tag molecule may quickly photobleach over time, losing its fluorescence due to photon induced chemical changes in its structure. The pathogen sensor proposed here does not suffer from these shortcomings.

5.2.2. Magnetic sensors. Some recent research efforts have focused on developing magnetic biosensors. The majority of these biosensing schemes have both the magnetic particles and the magnetic field sensor coated with the ligand. In these schemes, the target molecules act as a link between the magnetic particles and the magnetic field sensor, and their presence is detected via the stray magnetic field of the magnetic particles. Among such sensors are the beads array counter (BARC) [31], the Hall effect sensor [32], and spin valves [33]. While these sensing schemes can detect the concentration of the labelled magnetic particles and targets, they do not provide a direct measurement of the size of the target molecules. The sensor proposed in this paper provides both concentration and size information on the targets. Some other pathogen sensing schemes [34] depend on using functionalized magnetic microbeads to attach to specific target pathogens; these microbeads are then separated from the solution via an external permanent magnet and their 'loads' are analysed via various methods, including subsequent fluorescence imaging. In addition to being subject to the limitations of fluorescence detection mentioned above, this approach generally requires the skills of an experienced technician or researcher, and its sensitivity is limited. There exist pathogen detection schemes based on ferrofluids, as well. It is possible to detect changes in the Brownian relaxation time of nanoparticles via AC susceptometry [16, 17] or magneto-optical bifringence techniques [35]. The problem with the latter technique is that it requires an optical excitation and detection scheme, in addition to the magnetic excitation. The AC susceptibility measurements, on the other hand, are similar in their detection scheme and working principle to the ferrohydrodynamic pumping approach. The imaginary component of the magnetic fluid AC susceptibility has a peak very similar to the pumping peaks depicted in figure 16. In order for the scheme to work well, though, the magnetic field applied needs to be uniform over a sample volume and strong enough to almost saturate the ferrofluid. The sensor here, however, works in the small field/linear magnetization regime and the magnetic field applied need not (and is not) uniform across the length and the height of the microfluidic channel. Consequently, the resulting compact design of the proposed pathogen sensor, especially in miniaturized and integrated form, is relatively much simpler and more economical. The magnetic fields needed for the ferrohydrodynamic pumping approach are much lower than the fields utilized in the AC susceptometry measurement; consequently, they translate into much lower excitation currents—a fact that also simplifies the device design and thermal management.

6. Conclusion

Ferrohydrodynamic pumping via travelling waves offers very attractive possibilities for compact, reliable and integrated fluidic actuation schemes. In this work, we have considered both macro- and micro-scale device modelling, as well as simple initial experiments designed to test theory. Our main motivation is to demonstrate the feasibility of integrated micro-ferrofluidic devices, and especially their potential utility as highly sensitive integrated, disposable pathogen detector chips. In this context, a novel detection method based on multiple ferrohydrodynamic pumping peaks is proposed; this approach allows the detection scheme to be insensitive to viscosity and

temperature changes as a sample is introduced and mixed with the ferrofluid in a pathogen detection device.

Immediate future work will focus on the synthesis of composite ferrofluids, in order to test the overall sensitivity of the proposed pathogen detection scheme with various receptor–target combinations. The PCB substrates will also be replaced by silicon wafers for improved thermal management and the elimination of eddy-currents.

Acknowledgments

The authors would like to thank Professor Markus Zahn for insightful discussions. We are grateful to Professor Eric Dufresne for viscosity measurements and to Dr K Raj of Ferrotec for the ferrofluid sample. This work was in part supported by the National Science Foundation (ECS-0449264).

References

[1] Rosensweig R 1985 *Ferrohydrodynamics* (Cambridge: Cambridge University Press)
[2] Raj K and Moskowitz R 1990 *J. Magn. Magn. Mater.* **85** 233
[3] Shinkai M 2002 *J. Biosci. Bioeng.* **94** 606
[4] Pankhurst Q A, Connolly J, Jones S K and Dobson J 2003 *J. Phys. D: Appl. Phys.* **36** 167
[5] Park G S and Park S H 1999 *IEEE Trans. Magn.* **35** 4058
[6] Hatch A, Kamholz A E, Holman G, Yager P and Bohringer K F 2001 *J. Microelectromech. Syst.* **10** 215
[7] Yamahata C, Chastellain M, Parashar V K, Petri A, Hofmann H and Gijs M A M 2005 *J. Microelectromech. Syst.* **14** 96
[8] Love L J, Jansen J F, McKnight T E, Roh Y and Phelps T J 2004 *IEEE Trans. NanoBiosci.* **3** 101
[9] Zahn M and Greer D R 1995 *J. Magn. Magn. Mater.* **149** 165
[10] Mao L and Koser H 2004 *3rd Int. Conf. on Computational Modeling and Simulation of Materials (Sicily, Italy, 2004)* p 381
[11] Melcher J R 1981 *Continuum Electromechanics* (Cambridge, MA: MIT Press)
[12] Xia Y and Whitesides G 1998 *Ann. Rev. Mater. Res.* **28** 153
[13] Mao L and Koser H 2005 *J. Magn. Magn. Mater.* **289** 199
[14] Chaudhury M K and Whitesides G 1992 *Science* **255** 1230
[15] Mao L and Koser H 2005 *9th Int. Conf. on Miniaturized Systems for Chemistry and Life Sciences (μTAS) (Boston, MA, 2005)*
[16] Astalan A P, Ahrentorp F, Johansson C, Larsson K and Krozer A 2004 *Biosens. Bioelectron.* **19** 945
[17] Chung S H, Hoffmann A, Guslienko K and Bader S D 2005 *J. Appl. Phys.* **97** 10R101
[18] Zhao X, Hilliard L R, Mechery S J, Wang Y, Bagwe R P, Jin S and Tan W 2004 *Proc. Natl Acad. Sci.* **101** 15027
[19] van Honschoten J W, Svetovoy V B, Krijnen G J M and Elwenspoek M C 2005 *J. Microelectromech. Syst.* **14** 436
[20] Gupta A, Akin D and Bashir R 2004 *J. Vac. Sci. Technol.* B **22** 2785
[21] Jolivet-Reynaud C, Lesenechal M, O'Donnell B, Becquart L, Foussadier A, Forge F, Battail-Poirot N, Lacoux X, Carman W and Jolivet M 2001 *J. Med. Virol.* **65** 241
[22] Homola J, Sinclair S Y and Gauglitz G 1999 *Sensors Actuators* B **54** 3
[23] Leonard P, Hearty S, Brennan J, Dunne L, Quinn J, Chakraborty T and O'Kennedy R 2003 *Enzyme Microb. Technol.* **32** 3
[24] Peruski A H and Peruski L F 2003 *Clin. Diagn. Lab. Immunol.* **10** 506
[25] Shah J and Wilkins E 2003 *Electroanalysis* **15** 157
[26] Mirhabibollahi B, Brooks J L and Kroll R G 1990 *Appl. Microbiol. Biotechnol.* **56** 3278
[27] Koncki R, Radomska A and Glab S 2000 *Talanta* **52** 13
[28] Gerard M, Chaubey A and Malhotra B D 2002 *Biosens. Bioelectron.* **17** 345
[29] Weeks B L, Camarero J, Noy A, Miller A, Stanker L and De Joreo J 2003 *Proc. Nanotechnol.* **1** 123
[30] Brewster J, Gehring A G, Mazenko R S, Van Houten L J and Crawford C J 1996 *Anal. Chem.* **68** 4153
[31] Baselt D R, Lee G U, Natesan M, Metzger S W, Sheehan P E and Colton R J 1998 *Biosens. Bioelectron.* **13** 731
[32] Besse P A, Boero G, Demierre M, Pott V and Popovic R 2002 *Appl. Phys. Lett.* **80** 4199
[33] Ferreira H A, Graham D L, Freitas P P and Cabral J M S 2003 *J. Appl. Phys.* **93** 7281
[34] Rand A G, Ye J M, Brown C W and Letcher S V 2002 *Food Technol.* **56** 32
[35] Romanus E, Grob C, Kotitz R, Prass S, Lange J, Weber P and Weitschies W 2001 *Magnetohydrodynamics* **37** 328